Chapter 4

Investigations on the Higher order $HEM_{21\delta}$-like mode of the CDRA for cross-polarization reduction

4.1 Introduction

In the previous chapter, it was shown that the combination of the higher order $HEM_{21\delta}$ and the $TM_{01\delta}$ modes cause disturbances in the fundamental $HEM_{11\delta}$ mode radiation, resulting in high cross-polarization. In this chapter dual-feed mechanism is employed to excite the $HEM_{21\delta}$ mode, as the dominant radiating mode of the CDRA. Planar microstrip and slot technologies are adapted for the dual-feed, due to their compact geometry compared to the coaxial feed. The dual-feed geometry also excites the $TM_{01\delta}$ mode weakly, therefore the excited mode is correctly referred to as the $HEM_{21\delta}$-like mode. The analysis of the $HEM_{21\delta}$-like mode presented in this chapter is useful in three different ways – (i) it describes appropriate feeding techniques for exciting the $HEM_{21\delta}$-like mode dominantly, to be used as the operating mode (ii) provides a comparison between the microstrip and microstrip slot feeds in exciting the $HEM_{21\delta}$-like mode effectively (iii) it leads to the invention of $HEM_{21\delta}$-like mode suppression technique to lower the cross-polarization in the fundamental mode DRA.

4.2 Eigen Mode Analysis of the CDRA

Using the method described in chapter 1, the eigen mode analysis of the CDR ($\varepsilon_r = 24$, $\tan\delta = 0.002$, $2a = 19.43$ mm and $h = 7.3$ mm) is carried out with HFSS to identify the approximate operating frequency and the near-field pattern of the $HEM_{21\delta}$ mode for designing the feed geometry. By careful inspection of the modal field patterns at the respective eigen frequencies, the CDR modes are identified. To verify the modes further, accurate closed form equations available in the literature are used to compute the theoretical resonant frequencies of the above modes as follows:

$$HEM_{11\delta} \text{ [21]}: \quad f_0 = \frac{c}{2\pi a\sqrt{\varepsilon_r}}\left[1.71 + 2\left(\frac{a}{2h}\right) + 1.578\left(\frac{a}{2h}\right)^2\right] \qquad \ldots(4.1)$$

$$TM_{01\delta} \text{ [8]}: \quad f_0 = \frac{c}{2\pi a\sqrt{\varepsilon_r+2}}\sqrt{3.83^2 + \left(\frac{\pi a}{2h}\right)^2} \qquad \ldots(4.2)$$

$$HEM_{21\delta}\ [27]: \quad f_0 = \frac{1.03c}{2\pi a\sqrt{\varepsilon_r + 2}}\sqrt{3.83^2 + \left(\frac{\pi a}{2h}\right)^2} \qquad\qquad \ldots(4.3)$$

Eigen frequencies from HFSS simulations and corresponding theoretical values for the $HEM_{11\delta}$, $TM_{01\delta}$ and $HEM_{21\delta}$ modes are compared in Table 4.1, which shows decent agreement between the two methods confirming the modes. It can also be verified that the frequencies of the $HEM_{21\delta}$ mode and the $TM_{01\delta}$ mode are close to each other, implying a possible overlap when the $HEM_{21\delta}$ is excited in the DRA. The HFSS generated modal near-field patterns of the $TM_{01\delta}$ and the $HEM_{21\delta}$ are shown in the Fig. 4.1, which matches quite well with the computed patterns in [7]. Theoretical analysis of the $HEM_{21\delta}$ mode of a CDRA using the magnetic wall model predicts the radiation pattern with boresight-null in both the principle planes [65]. In a practical environment, exciting the $HEM_{21\delta}$ mode as in Fig. 4.1(b) recommends the use of a dual-feed mechanism with in-phase and equal amplitude feed currents. Such a feed configuration will also suppress the dominant $HEM_{11\delta}$ mode as it requires anti-phase feed currents. Although the source boundary condition for the $HEM_{21\delta}$ mode also favors the $TM_{01\delta}$ mode, the rotationally asymmetric dual-feed geometry will excite the $TM_{01\delta}$ mode only weakly. In the presence of the weak $TM_{01\delta}$ mode, the operating mode can be correctly termed as the $HEM_{21\delta}$-like mode. By superimposing the magnetic field patterns of both the above modes (Fig. 4.1 (a) and (b)), one can roughly predict the far-field behavior of the $HEM_{21\delta}$-like mode.

Table 4.1 Resonant frequencies of the CDR – HFSS Eigenmode vs Theory

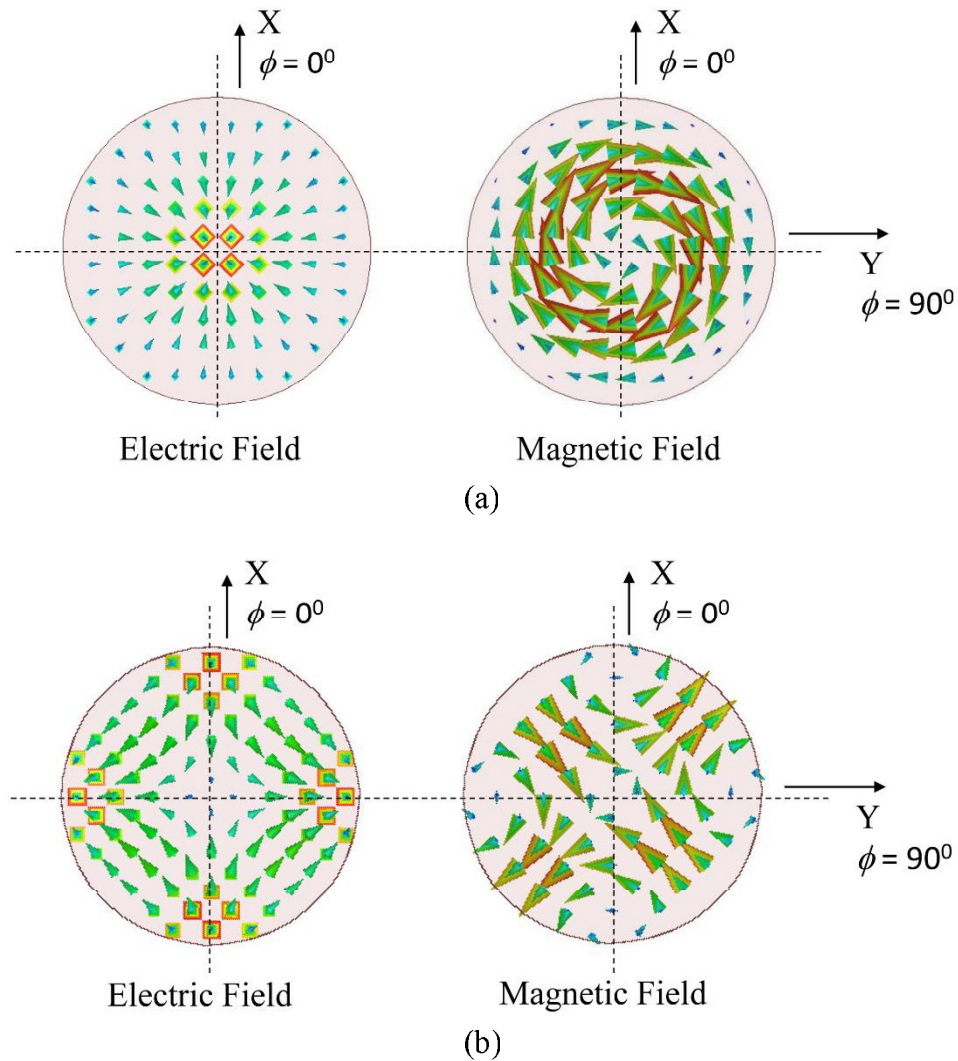| Mode	Resonant Frequency, GHz	
	HFSS	Theory
$HEM_{11\delta}$	3.028	3.12 [eq. (4.1)]
$TM_{01\delta}$	4.085	4.20 [eq. (4.2)]
$HEM_{21\delta}$	4.204	4.33 [eq. (4.3)]

Fig. 4.1 Top view of the E-field and the H-field intensities from the eigen mode analysis of the CDR for (a) $TM_{01\delta}$ mode (b) $HEM_{21\delta}$ mode

The superimposed modal field will be stronger in the $\phi = 0^0$ plane (due to constructive interference) and weaker in the $\phi = 90^0$ plane (due to destructive interference). However, such a mode mixing will not occur in the $\phi = 45^0$ and the $\phi = 135^0$ planes, due to the orthogonal alignment between the modal fields as can be seen in Fig. 4.1.

4.3 The Feed Designs

 The proposed dual-feed geometry can be realized using any of the standard feed mechanisms discussed in previous chapters. However, in this chapter, the planar feed strategies – (i) a dual-

microstrip feed and (ii) a dual-slot feed are considered. Design parameters that are common for both the feeds are shown in Table 4.2.

Table 4.2 Common design parameters of the two feed geometries

Parameter	Value
Substrate ε_r, tanδ	4, 0.02
Substrate height	1.6 mm
Ground plane size (L_G or W_G)	90 mm
Microstrip width (50 Ω)	3.22 mm
Microstrip width (100 Ω)	0.7 mm

4.3.1 Dual-microstrip feed

In this type of feed, a 50 Ω microstrip line is divided into two 100 Ω lines of equal length to excite the diametrically opposing feed points on the CDR with equal amplitude and phase, as required by the field profile of the HEM$_{21\delta}$ mode (Fig. 4.1(b)).
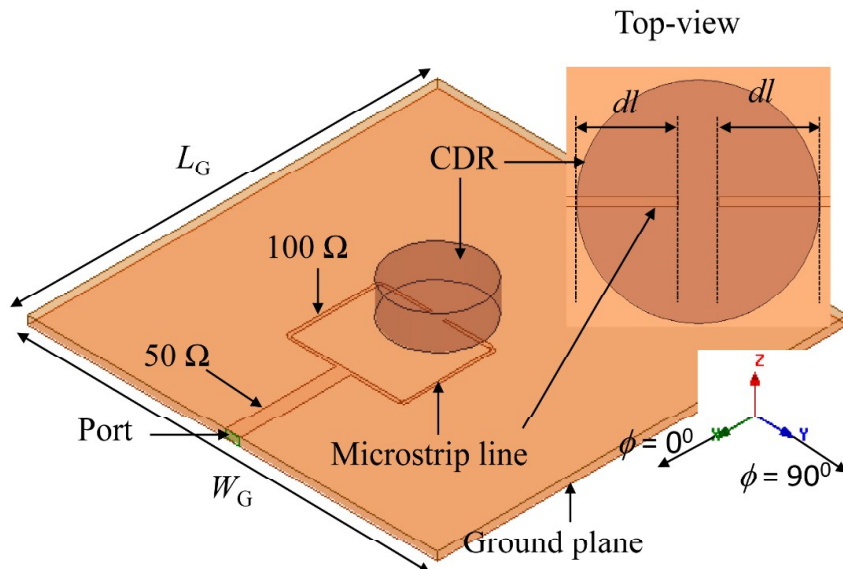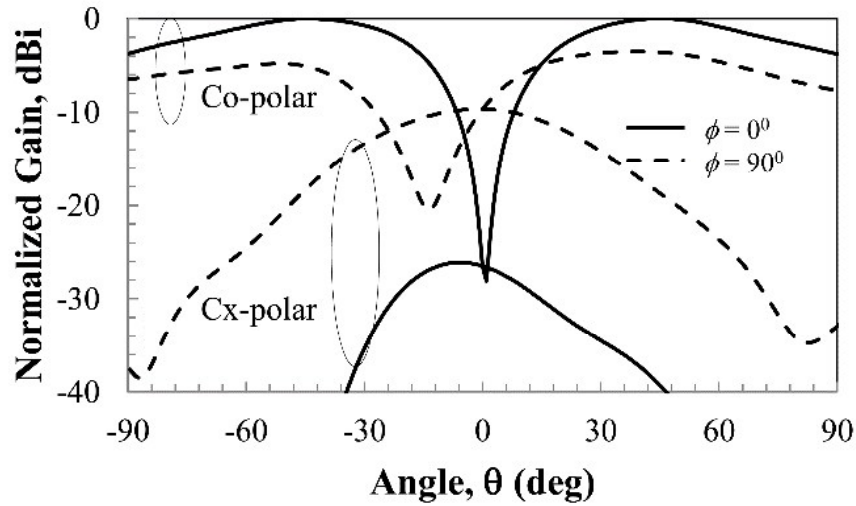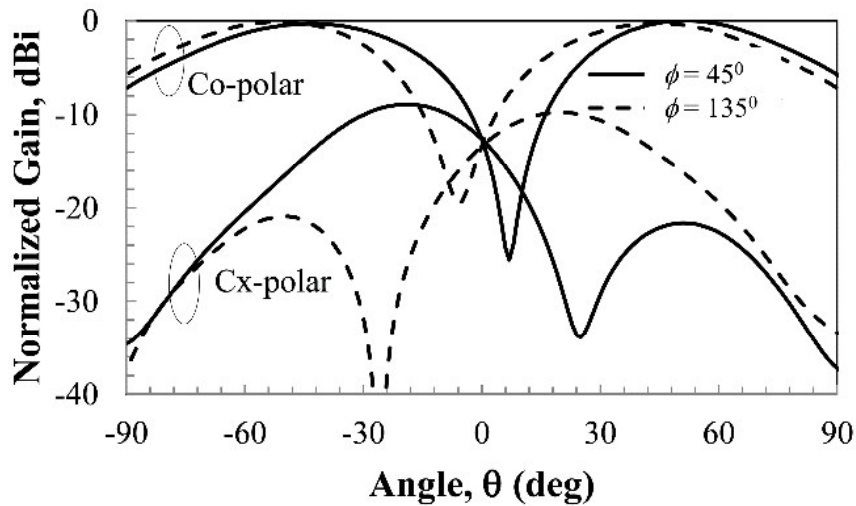

Fig. 4.2. HFSS model of dual microstrip fed CDRA

59

Fig. 4.3 Radiation patterns (HFSS) of the dual-microstrip fed CDRA (a) $\phi = 0^0$ and $\phi = 90^0$ planes (b) $\phi = 45^0$ and $\phi = 135^0$ planes

The HFSS model of the above feed is shown in Fig. 4.2. Impedance matching is achieved by varying the microstrip overlap length *dl* identically for both the feed lines as indicated in Fig. 4.2. For a ground plane size of L_G (or W_G) = 90 mm (~ 1.37λ_0), *dl* = 8.1 mm (~ 0.12λ_0) gives a resonant frequency of 4.583 GHz with reflection coefficient $|\Gamma_{in}|$ of −30 dB and bandwidth of 7.48 %. The resonant frequency is close to the value predicted in Table 4.1. Simulated radiation patterns in the four planes, $\phi = 0^0$, 45^0, 90^0 and 135^0 are shown in Fig. 4.3. Almost identical peak radiation levels are achieved in the $\phi = 45^0$ and $\phi = 135^0$ planes, while there is a difference

60

of about 3–5 dB in the radiation levels between the $\phi = 0^0$ and $\phi = 90^0$ planes. The above difference is thought of as the contribution from the $TM_{01\delta}$ mode as pointed out in section 4.2. The co-polar patterns show boresight-null radiation with peak gain 3.35 dBi as expected from the $HEM_{21\delta}$-like mode but the pattern asymmetry and the cross-polarization levels are very high due to spurious mode radiation [21], **[66]**.

4.3.2 Dual-slot feed

The dual-slot feed is constructed by etching two narrow slots on the ground plane of the dual-microstrip-feed as shown in Fig. 4.4. For a given slot position l from the center of the CDR and the slot size $W \times L$, the microstrip stub length dl' is adjusted for achieving impedance matching. Optimum slot position is found to be $l = 5$ mm ($\sim 0.09\lambda_0$), where the magnetic field lines of the $HEM_{21\delta}$ mode (Fig. 4.1(b)) is aligned in parallel with the slots.

The slot width is chosen as $W = 1$ mm ($\sim 0.02\lambda_0$) and the slot length is varied from $L = 9$ mm ($\sim 0.15\lambda_0$) to 12 mm ($\sim 0.20\lambda_0$). It is interesting to note that the stub length dl' required for impedance matching is invariant with L in the above range, giving an optimum value $dl' = 4.4$ mm ($\sim 0.08\lambda_0$). Radiation characteristics for various slot lengths are tabulated in Table 4.3. For $L = 11$ mm ($\sim 0.18\lambda_0$), the $HEM_{21\delta}$-like mode is excited at 4.996 GHz with maximum gain of ~ 3.6 dBi in both principal planes. The resonant frequency is higher than that predicted (Table 4.1) by about 700 MHz, as a consequence of the detuning caused by the dual-slots.
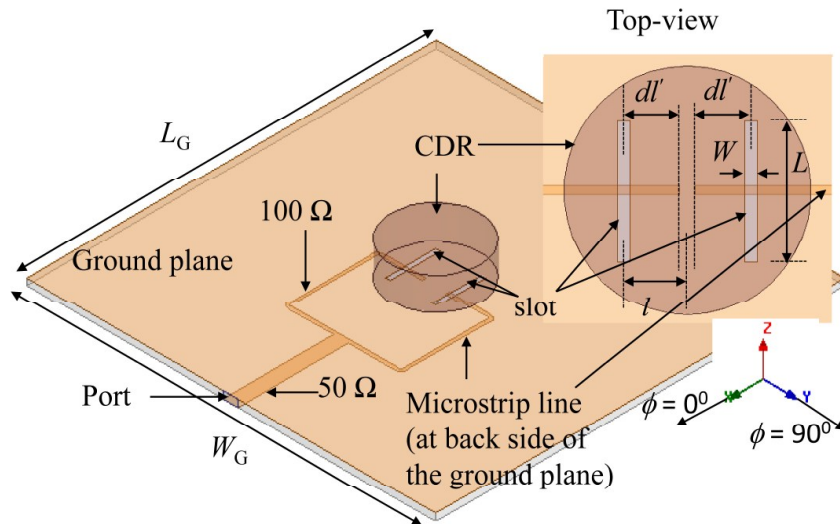

Fig. 4.4 HFSS model of the dual slot-fed CDRA

Table 4.3 Radiation characteristics of the dual-slot fed CDRA for varying slot length (*L*)

**(*W*=1 mm, *l* = 5 mm, and *dl'*= 4.4 mm)**

Slot length (*L*) for slot width (*W*)= 1 mm	f_0 (GHz)	$\|\Gamma_{in}\|$ (dB)	%Band-width	Max. ($\phi= 45^0$) gain (dB)	Max. ($\phi= 135^0$) gain (dB)	Max. ($\phi= 45^0$) cx-pol. level (dB)	Max. ($\phi= 135^0$) cx-pol. level (dB)
9	5.104	−29.54	4.23	3.36	3.13	−14	−14
10	5.041	−22.79	3.57	3.39	3.34	−15	−14
11	4.996	−16.90	3.10	3.63	3.60	−13	−12
12	4.960	−15.48	2.72	3.44	3.51	−13	−13

Table 4.4 Comparison of the performance characteristics of the HEM$_{21\delta}$ mode of the CDRA excited by the dual-microstrip feed (*dl* = 8.1 mm) and the dual-slot feed (*W* =1 mm, *L* = 11 mm, *l* = 5 mm, *dl'* = 4.4 mm)

| Parameter	f_0 (GHz)	$\|\Gamma_{in}\|$ (dB)	%Band-Width	Max. ($\phi= 45^0$) gain (dB)	Max. ($\phi= 135^0$) gain (dB)	Max. ($\phi= 45^0$) cx-pol. level (dB)	Max. ($\phi= 135^0$) cx-pol. level (dB)
Dual microstrip-fed CDRA	4.583	−38.36	7.48	3.29	3.35	−9	−10
Dual slot-fed CDRA	4.996	−16.90	3.10	3.63	3.60	−13	−12

Simulated radiation patterns are plotted in Fig. 4.5, where excellent symmetry in the $\phi = 45^0$ and $\phi = 135^0$ planes are achieved with peak gain of 3.6 dBi and cross-polar levels as low as − 13 dB. This improvement in the pattern symmetry of the dual-slot feed compared to that of the dual-microstrip feed is because of the isolation of the feed lines from the CDR [21], [66]. The radiation in the $\phi = 0^0$ and $\phi = 90^0$ planes are unequal for reasons that are the same as that for the dual-microstrip fed CDRA. Comparison between the above two excitation strategies for the HEM$_{21\delta}$-like mode is summarized in Table 4.4. As a result of the overall improvement in

the radiation performance of the $HEM_{21\delta}$-like mode when excited by the dual-slot feed, the same is considered for experimental validation.
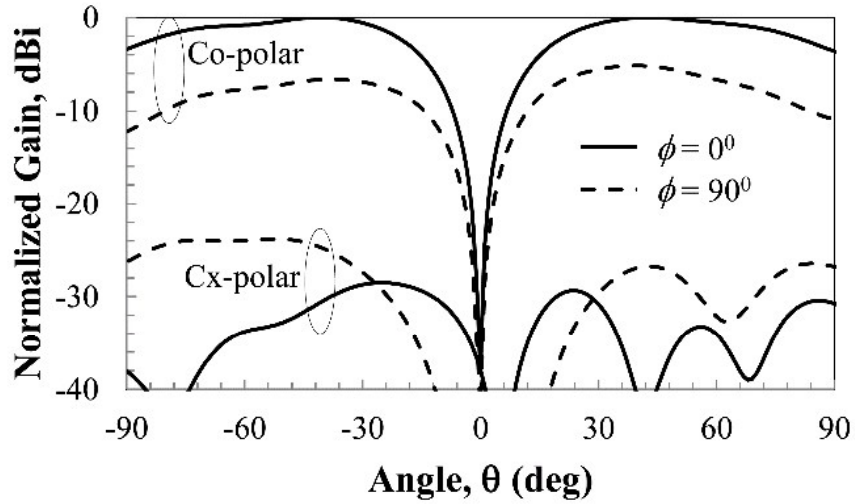
(a)
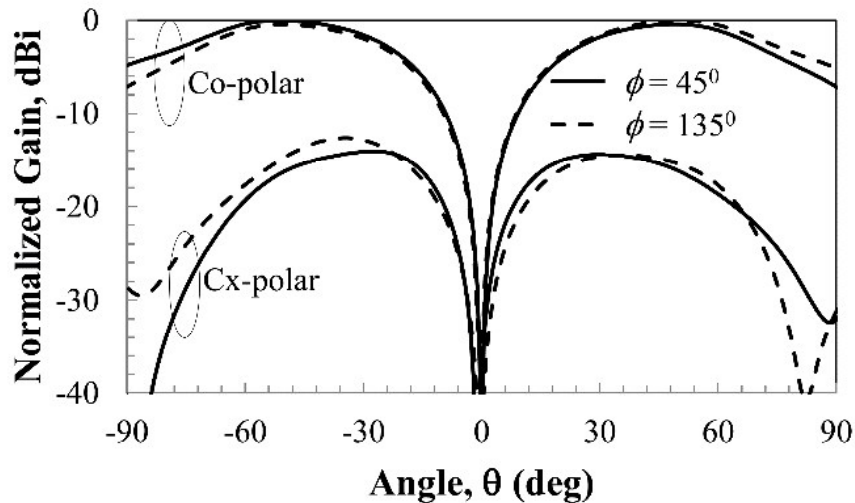
(b)

Fig. 4.5 Radiation patterns (HFSS) of the dual-slot fed CDRA (W×L = 1 mm × 11 mm, l = 5 mm, dl' = 4.4 mm) (a) $\phi = 0^0$ and $\phi = 90^0$ planes (b) $\phi = 45^0$ and $\phi = 135^0$ planes

4.4 Experimental Results

Photograph of the dual-slot fed CDRA prototype is shown in Fig. 4.6 which is characterized as described in chapter 1. Measured and simulated reflection coefficients of the CDRA are shown in Fig. 4.7. Figure shows that the desired $HEM_{21\delta}$-like mode is excited at 4.966 GHz in

measurement which is in good agreement with the simulated frequency of 4.996 GHz. In fact, there appears a resonance at 3 GHz in simulation and 3.4 GHz in measurement as clear from Fig. 4.7. From the simulated near-field patterns at 3 GHz, this first resonance is identified as the non-radiating mode of the CDR loaded slot, and the 400 MHz difference between the simulation and measurement is due to the fabrication errors of the slot. This error however does not reflect remarkably in the second resonance which is mostly decided by the properties of the CDR (ε_r, $2a$ and h) which are constants in both simulation and measurement. Measured versus simulated radiation patterns of the dual-slot fed CDRA for $\phi = 45^0$ and 135^0 planes are shown in Fig. 4.8.
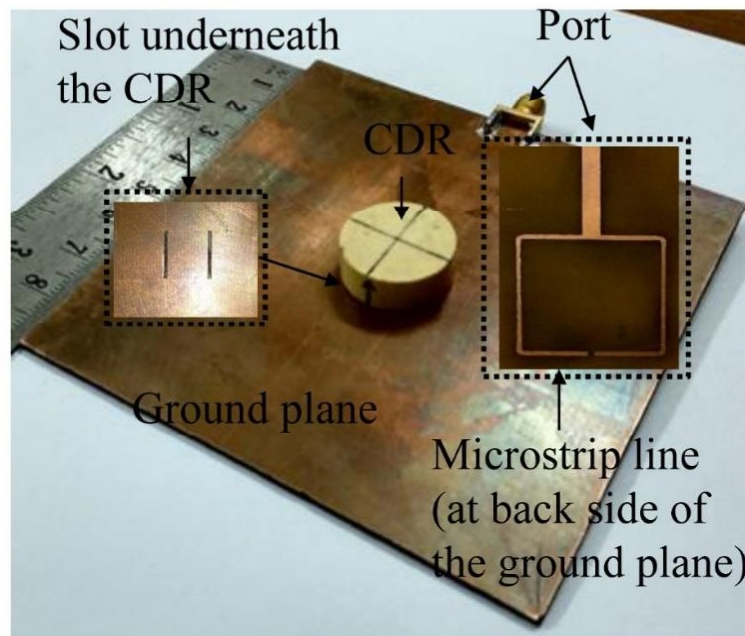
Fig. 4.6 Fabricated prototype dual-slot fed CDRA

Broadside-null radiation as expected for the $HEM_{21\delta}$-like mode is observed in the measurement also. Measured and simulated peak gain versus frequency of the dual-slot fed CDRA is plotted in the Fig. 4.9. Major DRA characteristics are presented in Table 4.5, which show that all the measured results are in good match with the simulated results. Small mismatches between the measured and the simulated characteristics are due to the errors in the fabrication of the slots and in the alignment of the CDR with respect to the slots.

Table 4.5 Simulated and measured characteristics of the dual-slot fed CDRA

Parameter	f_0 (GHz)	$|\Gamma_{in}|$ (dB)	%Band-Width	Max. (ϕ= 45^0) gain (dB)	Max. (ϕ= 135^0) gain (dB)	Max. (ϕ= 45^0) cx-pol. level (dB)	Max. (ϕ= 135^0) cx-pol. level (dB)
Simulated	4.996	−16.90	3.10	3.63	3.60	−13	−12
Measured	4.966	−26.71	4.40	3.45	3.31	−12	−11
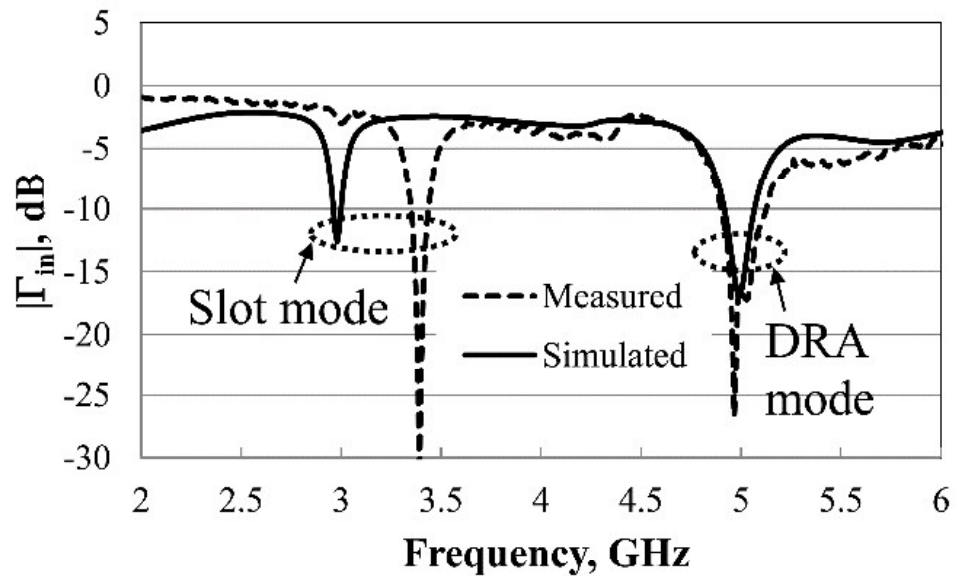
Fig. 4.7 Measured versus simulated reflection coefficient of the dual-slot fed CDRA (W×L = 1 mm × 11 mm, l = 5 mm, dl' = 4.4 mm)

To further confirm the nature of the two resonances found in Fig. 4.7, the magnetic field intensity patterns (H-field in A/m) in the CDR are generated with HFSS as furnished in Fig. 4.10. As shown in Fig. 4.10 (a), at the first resonance of 2.98 GHz, the field is concentrated in the slots implying that the resonance is caused by the slots loaded by the CDR. At the second resonance of 4.996 GHz, the field is contained in the CDR volume as shown by Fig. 4.10 (b), confirming it the CDR mode. In addition, Fig. 4.10 (b) shows stronger fields in the ϕ= 0^0 plane, while weaker field at the ϕ = 90^0 plane, as it was qualitatively interpreted in section 4.2, confirming the excitation of the $HEM_{21\delta}$-like mode by the dual-slot feed.
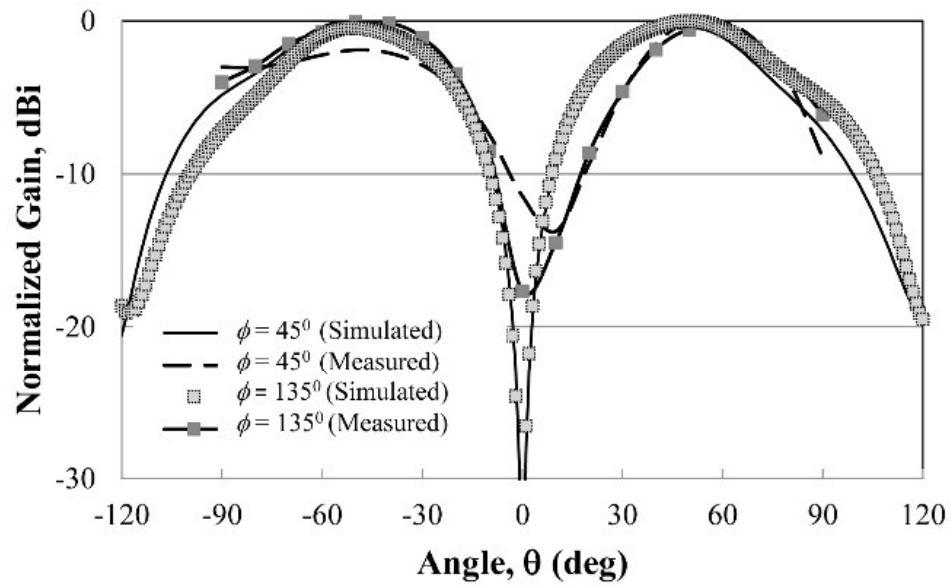
65

Fig. 4.8 Measured versus simulated co-polar radiation patterns (normalized) of the dual-slot fed CDRA (W × L = 1 mm × 11 mm, l = 5 mm, dl' = 4.4 mm) in the $\phi = 45^0$ and 135^0 planes
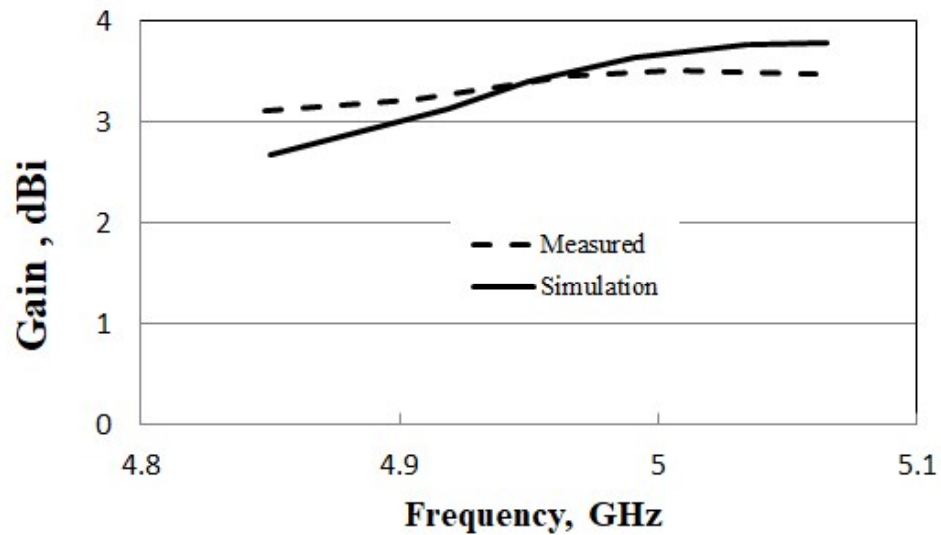
Fig. 4.9 Measured and simulated peak gain versus frequency of the dual-slot fed CDRA (*W×L* = 1 mm × 11 mm, *l* = 5 mm, *dl'* = 4.4 mm)
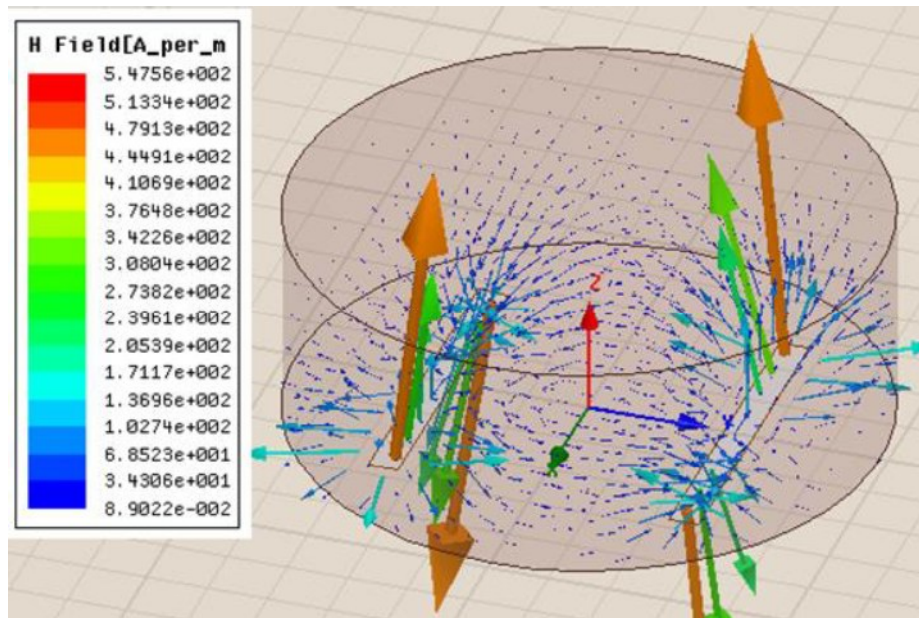
(a)
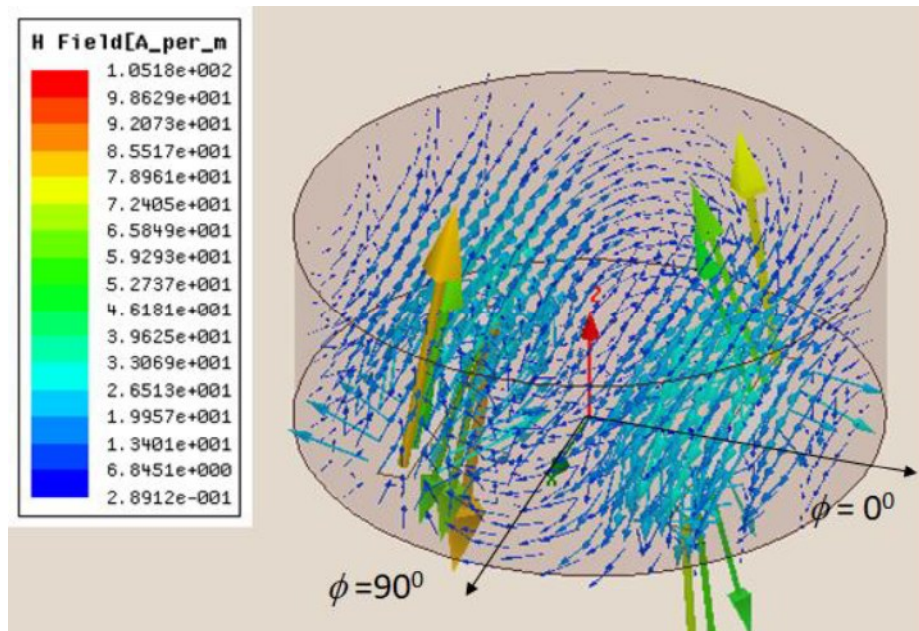
(b)

Fig. 4.10 Near-field (H-field in A/m) pattern (HFSS) of the dual-slot fed CDRA (W × L = 1 mm × 11 mm, l = 5 mm, dl' = 4.4 mm) at (a) 2.98 GHz (Slot mode) (b) 4.996 GHz (CDR mode)

4.5 Effect of External Perturber on the $HEM_{21\delta}$-like mode

The DRA being a dielectric body allows loading metallic perturbers in the form of posts, pins and strips to manipulate its modes. Use of internal perturbers [27], [40], [41] poses fabrication challenges. So in this work, a parasitic metal strip made from a conducting copper tape is judiciously wrapped on the CDR to greatly influence the $HEM_{21\delta}$-like modes through shorting out its E-fields present on the surface of the CDR. This is experimentally demonstrated on the dual-slot fed CDRA prototype as shown in Fig. 4.11. The metal strip of width 3 mm is adhered on the CDR along the diameter perpendicular to the polarization of the $HEM_{11\delta}$ mode. This will ensure the $HEM_{11\delta}$ mode minimally affected if it is also present in the DRA (in fact this is true in the fundamental mode DRA). Fig. 4.12 shows the measured reflection coefficient with and without metal strip wrapping which clearly shows the suppression of the $HEM_{21\delta}$-like resonance. The new resonance dip is centered at around 5.34 GHz but its magnitude is suppressed by 18 dB from that of the CDRA without metal strip. In addition, it is also observed from simulations that the strip loading reduces the peak gain in the new band by 2.11 dB compared to that without metal strip. Therefore, this design strategy is incorporated in the fundamental mode ($HEM_{11\delta}$ mode) CDRA design using microstrip feed.
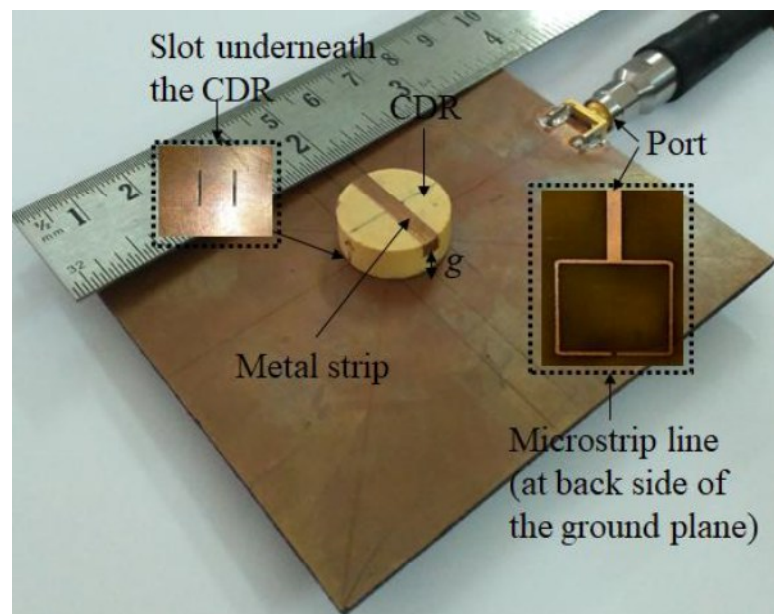

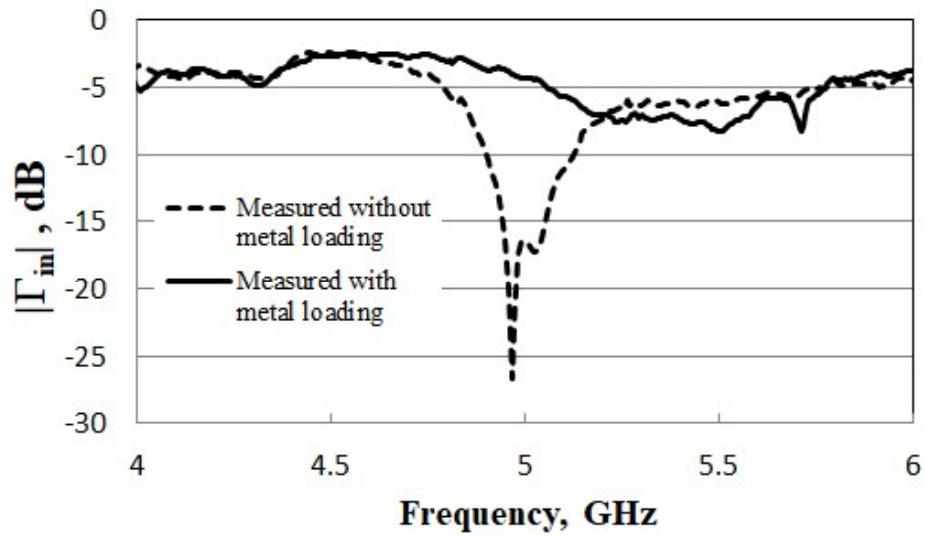Fig. 4.11 Prototype of the dual-slot fed CDRA with metal strip wrapping on the CDR

Fig. 4.12 Measured reflection coefficient of the dual-slot fed CDRA (W×L = 1 mm × 11 mm, l = 5 mm, dl' = 4.4 mm) with and without the metal strip wrapping (g = 1 mm)

4.6 Microstrip fed CDRA with Metal Strip Wrapping

The DRA geometry is shown in Fig. 4.13 (a) and (b). Basic design parameters of the microstrip fed CDRA is identical to that in chapter 3.

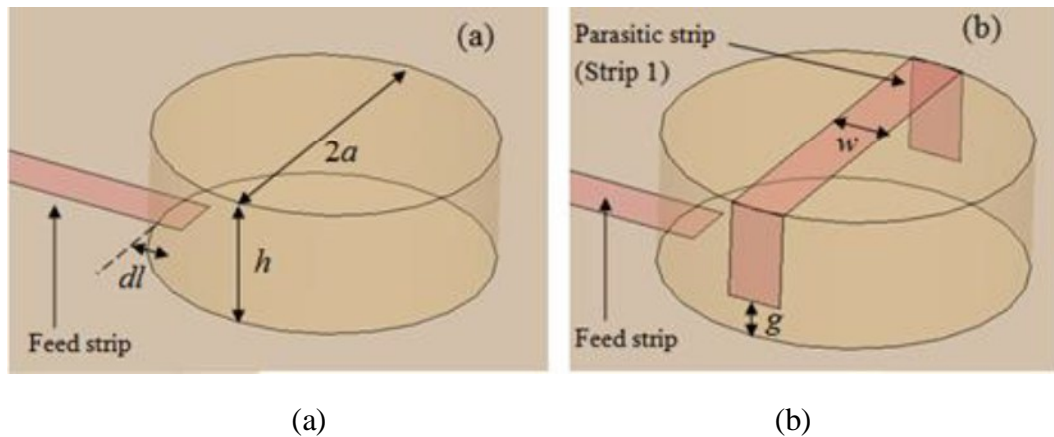(a)   (b)

Fig. 4.13 Microstrip fed DRA designs (a) Without strip (b) With strip (Only the top side of the substrate is shown)

As shown, the CDR is partially wrapped with a conducting strip of width w leaving a gap g between the strip end and the CDR as indicated in Fig. 4.13 (b).

For the basic DRA without the strip or $w = 0$ (Fig. 4.13 (a)), a resonant frequency of $f_0 =$ 3.44 GHz with reflection coefficient $|\Gamma_{in}| = -39$ dB is achieved. When the strip is loaded on the CDR as shown in Fig. 4.13 (b), the operating resonance of the DRA is detuned proportional to the strip width w, as w is tangential to the co-polarized electric (E) field of the $HEM_{11\delta}$ mode on the top surface of the CDR. Thus $w = 3$ mm is chosen for which $f_0 = 3.37$ GHz and $|\Gamma_{in}| =$ -30 dB, indicators of very less deterioration compared to $w = 0$. Now the strip gap parameter g which decides the total strip length $2(h+a-g)$ as in Fig. 4.13(b) is varied. However, the above variation doesn't change the resonant frequency because, the strip length along the CDR side wall of height $h-g$ (w.r.t Fig. 4.13 (a) & (b)) causes ideally no perturbing effects on the $HEM_{11\delta}$ mode, as there is zero tangential E-field along h at $\phi = 90^0$ with respect to the feed point. However, for any other mode polarized in the orthogonal plane such as the $HEM_{21\delta}$ mode, the strip length will have a significant shorting effect. The H-plane radiation patterns for various g are shown in Fig. 4.14, which indicates that, for $g = 2$ mm, the peak cross-polar radiation is
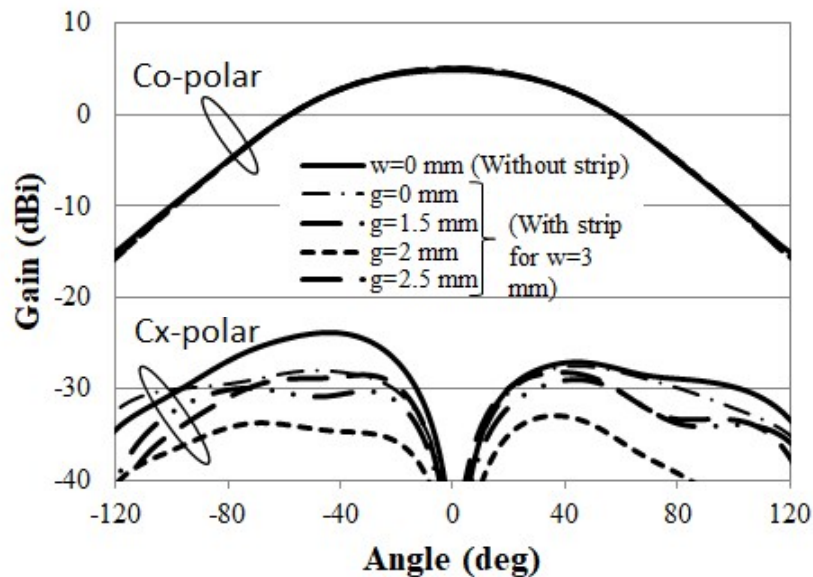

Fig. 4.14 Simulated H-plane radiation patterns for the CDRA without and with strip loading ($dl = 2$ mm, $w = 3$ mm). Without strip DRA ($w = 0$) pattern is plotted at 3.44 GHz and all others at 3.37 GHz
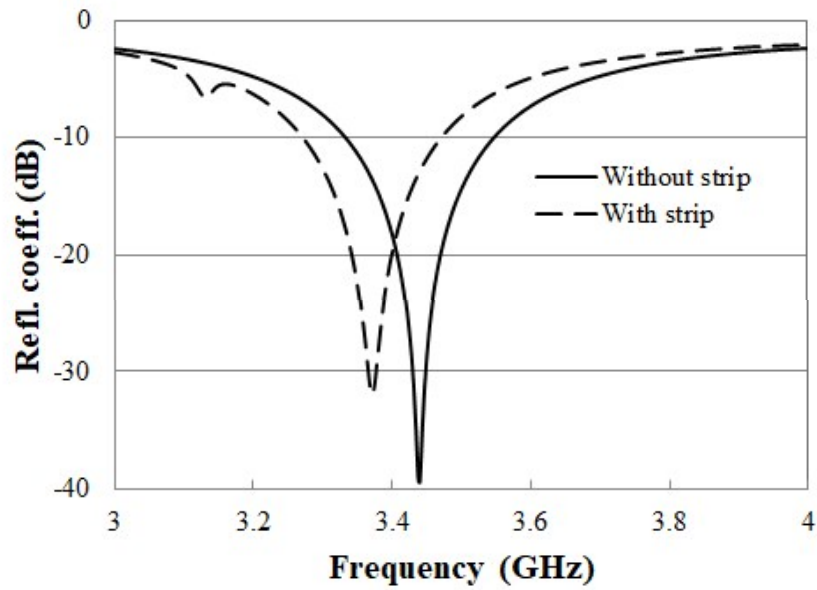
Fig. 4.15 Simulated reflection coefficients of CDRA without and with strip loading ($dl = 1.7$ mm, $w = 3$ mm, $g = 2$ mm)
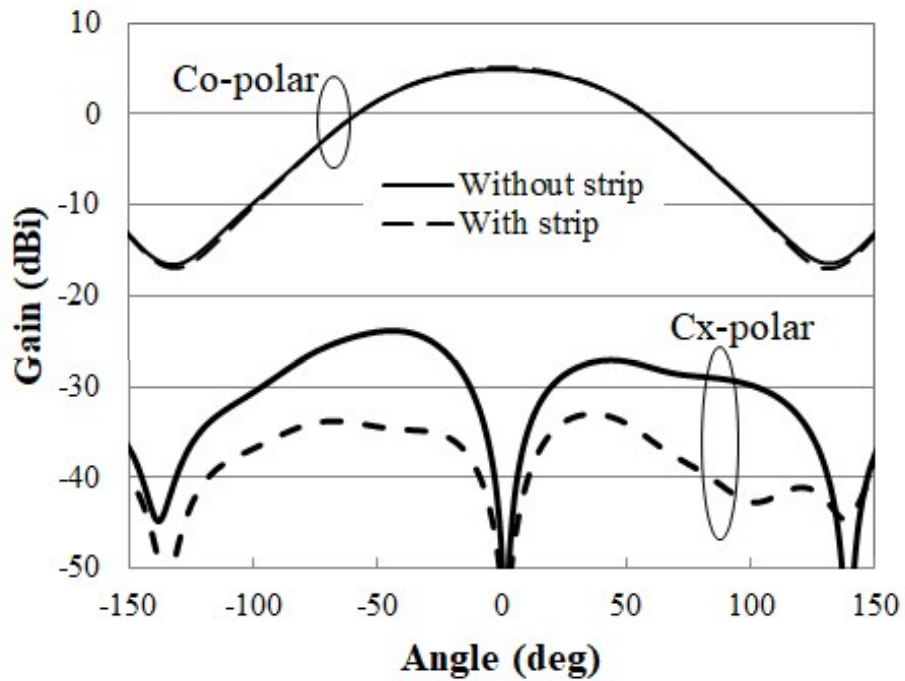

Fig. 4.16 Simulated H-plane radiation patterns of CDRA without strip at 3.44 GHz and with strip loading at 3.37 GHz ($dl = 2$ mm, $w = 3$ mm, $g = 2$ mm
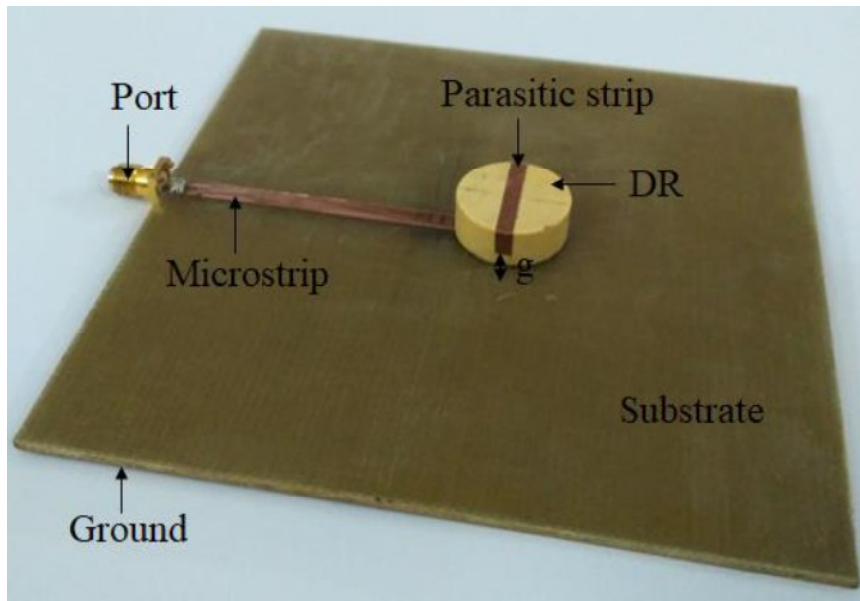
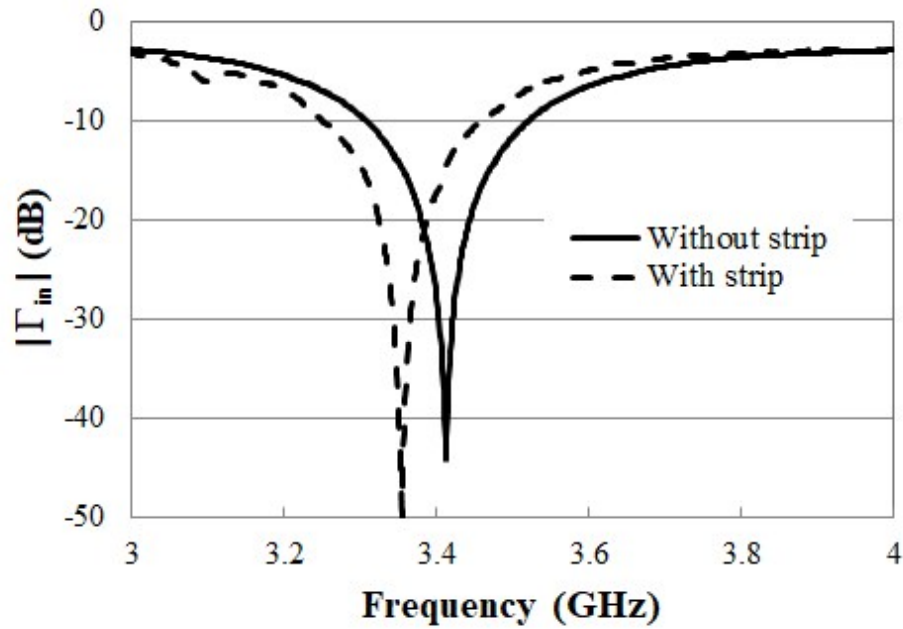Fig. 4.17 Photograph of the fabricated prototypes of CDRA with strip loading

Fig. 4.18 Measured reflection coefficients ($|\Gamma_{in}|$) of CDRA without strip and with strip loading

($dl = 1.7$ mm, $w = 3$ mm, $g = 2$ mm)

reduced by about 9 dB with respect to the basic DRA. For the optimized design ($g = 2$ mm), the reflection coefficients of the DRA are compared in Fig. 4.15 and the H-plane radiation patterns in Fig. 4.16. In the radiation patterns, about 9 dB reduction in the peak cross-polar gain is clearly observed for the DRA with strip loading. Photograph of the fabricated prototype of the strip loaded DRA is shown in Fig. 4.17. Measured reflection coefficient plots are shown in Fig. 4.18. The resonant frequencies are 3.41 GHz and 3.36 GHz respectively for before and after strip loading, which are in very good agreement with the simulated results (3.44 GHz and 3.37 GHz respectively). But, the simulated improvement in the cross-polarization was not observed in the measurements. It is true that the cross-polar radiation is highly sensitive to alignment and positioning errors that arise in antenna measurements [64], [67].

In the present design, the parasitic strip parameters such as the strip gap (g) and its alignment with respect to the center of the CDR which were decided manually, could have been the reason for the mismatch. Therefore, a better cross-polar reduction technique that does not interact directly with the CDR, but with its radiated fields is discussed in the next chapter.

4.7 Conclusion

In this chapter, the radiation performance of the $HEM_{21\delta}$ mode of a CDRA utilizing planar feeding techniques was investigated. A comparative study between a dual-microstrip feed and a dual-slot feed revealed that the latter excited the $HEM_{21\delta}$ mode with better modal purity, quantified by better pattern symmetry and lower cross-polarization. A prototype of the dual-slot fed CDRA was fabricated and tested to confirm the predicted performance. Further, near-field analysis in HFSS was carried out to verify the excited mode. If the radiation pattern of the $HEM_{21\delta}$-like mode DRA is compared with that of the $TM_{01\delta}$ mode DRA (another HOM of a CDRA), it can be observed that both radiates with a broadside null. Also, the former radiates usefully only in selected planes with peak gain < 4 dBi, whereas the latter radiates omni-directionally with gain ~ 6 dBi, comparable to the $HEM_{11\delta}$ mode. Thus the $HEM_{21\delta}$ mode is not recommended for general communication applications, which however has alternate applications [58]. The characterization of the $HEM_{21\delta}$-like mode also proved useful in designing its suppression methods. Parasitic metal strip wrapping on the DRA body was shown to be an effective suppression technique. For optimum strip design, about 9 dB improvement in the

cross-polar level was achieved in simulation. However, this method was found very sensitive to changes in the strip dimensions and its alignment with respect to the CDR. Therefore, a better technique of substrate / ground plane size optimization for cross-polarization minimization will be explored in the next chapter.